Journal of Applied Geophysics 245 (2026) 106025

Contents lists available at ScienceDirect

Journal of Applied Geophysics

journal homepage: www.elsevier.com/locate/jappgeo

# Interpretation of corrected sea floor HVSR data on a gas emitting structure in the Sea of Marmara

A. Brindisi [a,b], S. D'Amico [c,d], L. Beranzoli [c], D. Embriaco [c], A. Giuntini [c], D. Albarello [a,e,*]

[a] Dipartimento di Scienze Fisiche, della Terra e dell'Ambiente, Università degli Studi di Siena, Siena, Italy
[b] Museo Nazionale dell'Antartide "Felice Ippolito", Università degli Studi di Siena, Siena, Italy
[c] Istituto Nazionale di Geofisica e Vulcanologia, Sezione Roma2, Roma, Italy
[d] Università di Catania, Dipartimento di Scienze Biologiche, Geologiche e Ambientali, Sezione di Scienze della Terra, Catania, Italy
[e] Consiglio Nazionale delle Ricerche, Istituto di Geologia Ambientale e Geoingegneria, Rome, Italy

ARTICLE INFO

*Keywords:*
Ocean bottom seismic noise
H/V spectral ratios
Ambient vibrations
Gas emitting structures
Biot-Gassmann theory

ABSTRACT

Ocean bottom measurements of ambient vibrations at a gas emitting area in the Marmara region are analyzed. The overall stability of average Horizontal to Vertical Spectral Ratios (HVSR) of ambient vibrations values above 0.2 Hz obtained in different sea conditions suggests that the relevant pattern is weakly affected by oceanic disturbances and can be considered informative about the subsoil structure. A procedure based on the removal of the water column effect from sea floor HVSR data is illustrated which allows the application to off-shore data of inversion tools developed for inland measurements. On this basis, sea floor HVSR measurements are used to tentatively constrain the local seismostratigraphical configuration in terms of $V_s$ and $V_p$ profiles. On this basis three main seismic impedance contrasts have been identified (respectively around 10, 100 and 500 m below the sea floor) in good correspondence with geological unconformities revealed by seismic reflection data. Moreover, the interpretation of the body wave profiles and, in particular, of the $V_s/V_p$, ratios suggest the presence of unconsolidated material down to a depth of about 500 m below the sea level with an estimated porosity of the order of 30 %. Based on the Biot-Gassmann model, the body wave profile has been used for a preliminary estimate of the degree of gas saturation which reaches 70 % in the depth range 150–500 m of depths below the sea floor. Beyond these figures, results obtained suggest that a methodology base on the interpretation of HVSR data at sea bottom may represent a new important tool for the characterization of the sea bottom subsoil structure in correspondence of gas reservoirs.

## 1. Introduction

In recent years, several studies have suggested that measurements of ambient vibrations could provide useful insights into the location and characteristics of hydrocarbon reservoirs (e.g., Lambert et al., 2007; Saenger et al., 2009).

Specific signatures HVSR has been also evidenced relative to inland gas reservoirs corresponding to mud volcano fields in Italy (Antunes et al., 2022; Brindisi et al., 2025; Grassi et al., 2022; Panzera et al., 2016). This kind of measurements (for an extensive methodological review see Molnar et al., 2022) has been widely used worldwide as a fast and effective tool for the subsoil seismic characterization inland in many different contexts (e.g., Mele et al., 2021; Comina et al., 2023; Keskinsezer et al., 2023). To exploit HVSR data for subsoil prosecting, several numerical inversion procedures have been proposed and implemented which allow to constrain the body wave velocity profile (e.g., Herak, 2008; García-Jerez et al., 2016; Bignardi et al., 2016; Wathelet et al., 2020). These procedures rely on different forward models, each considering different properties of the ambient vibration wavefield. Albarello et al. (2023) has shown that, when applied in controlled situations, the best performing procedures are the one based on the hypothesis that the ambient vibrations results from a diffuse wavefield (Sánchez-Sesma, 2017) and the one based on the hypothesis that uprising body waves dominated the field (Herak, 2008): both appear effective in most cases, despite the strong differences in the underlying physical models. None of these numerical procedures, however, can be

* Corresponding author at: Dipartimento di Scienze Fisiche, della Terra e dell'Ambiente, Università degli Studi di Siena, Siena, Italy.
*E-mail addresses:* albachiara.brindi@student.unisi.it (A. Brindisi), salvatore.damico2@ingv.it (S. D'Amico), laura.beranzoli@ingv.it (L. Beranzoli), davide.embriaco@ingv.it (D. Embriaco), alessandra.giuntini@ingv.it (A. Giuntini), dario.albarello@unisi.it (D. Albarello).

https://doi.org/10.1016/j.jappgeo.2025.106025
Received 30 July 2025; Received in revised form 12 October 2025; Accepted 9 November 2025
Available online 17 November 2025

applied to sea bottom observations. One can expect that, in this condition, the presence of a water column above the measuring tool plays an important role which cannot be ignored. Actually, few applications of these ambient vibrations to constrain local stratigraphy have been provided based on sea bottom observations (Huerta-Lopez et al., 2003; Muyzert, 2007; Overduin et al., 2015). Some attempts have been also provided by considering HVSR data approach (Shynkarenko et al., 2021; Farazi et al., 2023) based on the diffuse wavefield model adapted to sea floor conditions by Lontsi et al. (2019). This approach appears numerically troublesome, and no shareware software has been made available which implements this approach into a numerical inversion tool. Moreover, when a marked anisotropy of the ambient vibration wavefield exists (which the case of many seabottom conditions) the safe application of this model, which assumes the perfect isotropy of the wavefield, is prevented (see, e.g., Mulargia, 2012). An alternative approach recently proposed by Albarello (2025) will be applied the following, which is based on the body waves model by Herak (2008) and allows the application of the well-established inversion procedure implemented by Bignardi et al. (2016). In particular, this procedure has been applied to constrain the subsoil configuration of the gas emitting structure corresponding to the submerged westernmost edge of the North Anatolian Fault (NAF) in the İzmit Gulf area (Eastern Mediterranean), where methane seepage from the seabed is present (Embriaco et al., 2014).

In the following sections, the key characteristics of the study area are first described, drawing on findings from prior multidisciplinary studies conducted in this field. Subsequently, ambient vibration data collected at the seabed are examined by focusing on HVSR. The hypothesis is that this information is more representative of the subsoil structure and nearly unaffected by the oceanic activity. HVSR data obtained by seismic observation are then inverted to constrain the seismostratigraphical configuration at the measurement site along with the main gas reservoir features.

## 2. Geological setting

The northern branch of the NAF enters the İzmit Gulf at the eastern margin of the Sea of Marmara (Fig. 1), forming a sequence of ridges and depressions on scales ranging from a few hundred meters to several kilometres (Polonia et al., 2004; Kurt and Yücesoy, 2009). Gas bearing sediments are widespread throughout the İzmit Gulf (Kuşçu et al., 2005; Gasperini et al., 2012) and the fault zones act as drainage conduits for the gas-bearing deposits, as confirmed by a gas-geochemical survey, where the highest values of dissolved methane in the bottom waters

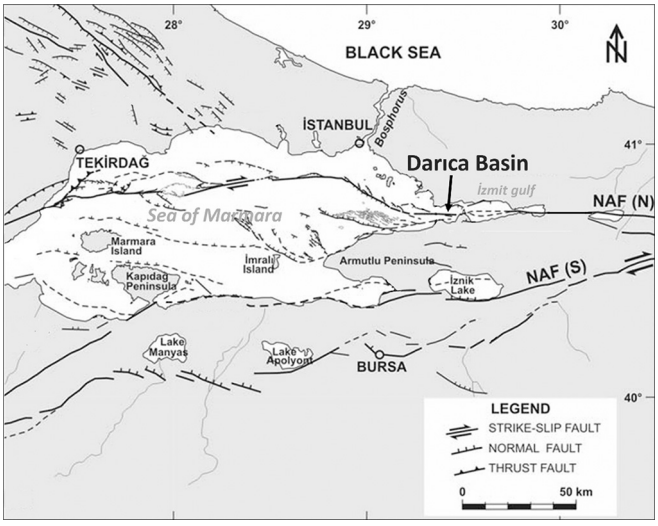


**Fig. 1.** Tectonic map of the Marmara region modified from Okyar et al., 2008.

were found near the main NAF trace (Gasperini et al., 2012). Along this structure, gas-rich sediments and cold seeps exist releasing microbial methane into the seawater (Gasperini et al., 2012). The present study focuses on the Darıca Basin, a shallow water inlet connecting the gulf to the main basins of the Marmara Sea (Fig. 1). High resolution seismic reflection data relative to the off-shore stratigraphy of this area indicates the presence of three distinct depositional sequences (Okyar et al., 2008; Kurt and Yücesoy, 2009) identified by the presence of conformable reflectors, bounded above and below by unconformities (Mitchum et al., 1977). Borehole data indicate the muddy, sandy, and gravelly nature of these sediments (Çetin et al., 1995; Okyar et al., 2008). At the top of the sequence there are Holocenic deposits bounded below by a clear reflector and above by the present-day seafloor. The thickness varies between 10 and 25 m (Gasperini et al., 2012). Below this layer two pre-Holocenic sedimentary sequences are present, separated from the overlying Holocene by a prominent erosional reflector. The first of this sequence reaches a maximum thickness of about 80 m (Kurt and Yücesoy, 2009) and is bounded at the bottom by a clear unconformity. Seismic data do not allow estimating the thickness of the older sequence below.

## 3. Seismic observations

A multi-parameter benthic observatory (SN-4) of GEOSTAR class (Favali et al., 2006) was deployed at the entrance of the İzmit Gulf (40°43.7452′ N, 29°23.2394′ E), operating for about six months at a depth of 166 m (Embriaco et al., 2014). SN-4 included a three-component broadband seismometer, as well as gas sensors ($CH_4$, $O_2$) and oceanographic sensors (single-point three-component current meter, turbidity meter, and CTD). The observatory stability was verified just after the touch-down and during the entire mission. The seismometer was deployed following a well-established procedure to guarantee a good seafloor coupling and minimizes disturbances induced by the observatory (Beranzoli et al., 2003; Monna et al., 2005; Favali et al., 2006).

SN-4 was deployed at the western end of the İzmit Gulf, along the main displacement zone of the NAF, in an area where relatively weak or potential seepage flows could be recorded. A detailed description of the campaign and of relevant outcomes relative to gas seepage monitoring are reported by Embriaco et al. (2014).

Part of the seismic data set has been re-examined by focusing on horizontal to vertical spectral ratios of ambient vibrations. To this purpose, seismic observations have been considered relative to three distinct time intervals of varying durations: October 21, 2009 (24 h), December 1, 2009 (24 h), and March 10–13, 2010 (72 h). The aim of this selection is evaluating the stationarity of HVSR curves during different meteoclimatic and oceanographic conditions. Observations relative to each hour within each of the considered time intervals have been processed separately by following Picozzi et al. (2005). Specifically, the single components spectra were computed by averaging 20 s long time non-overlapping windows; a baseline correction and a 5 % cosine taper were applied to each window, and the spectra were smoothed using a triangular moving window with a frequency-dependent half width (20 % of central frequency). Based on this parametrization, the ratios of average spectral amplitudes of ambient vibrations measured along the vertical and horizontal directions of ground motion have been computed at each frequency to obtain the HVSR curve (e.g., Molnar et al., 2022) in the frequency range 0.1–10 Hz.

An example of the outcomes of this analysis is shown in Fig. 2, relative to October 21st 2009. In the range of interest for the present study, spectra of ambient vibrations show two prominent peaks (approximately 0.3 and 0.6 Hz) along the three components in the frequency range of secondary microseisms (e.g., Webb, 1998; Lepore and Grad, 2020). These are caused by pressure variations on the seabed induced by the amplitude changes of surface wave motion (Longuet-Higgins, 1950; Hasselmann, 1963) related to long-period waves generated by wind motion and their mutual interference. By following Nakata

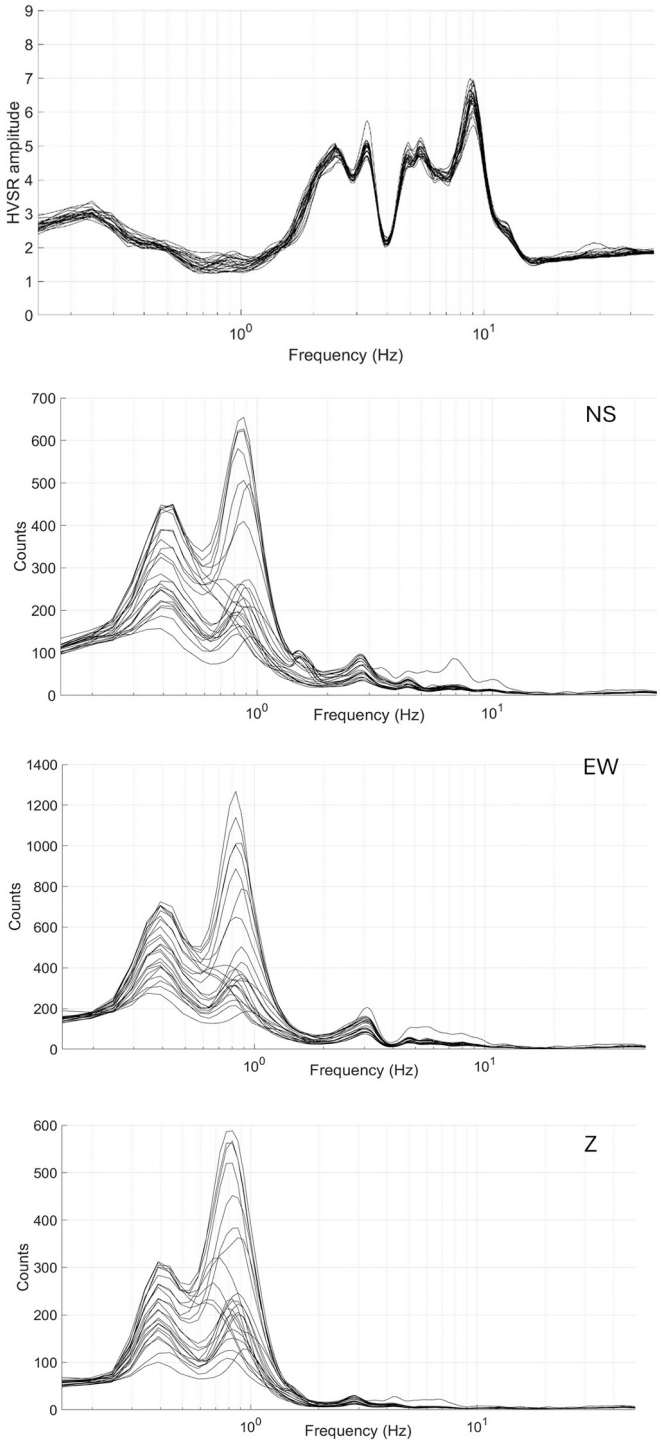


**Fig. 2.** Spectral structure of ambient vibrations relative to Ocean Bottom Seismometer (OBS) measurements during October 21st 2009. In the upper inset, the HVSR curves relative to 1 h time windows are reported. The subsequent plots report the power spectra of ambient vibrations along the three ground motion components during the same time windows.

et al. (2019), typical frequency $\nu$ of sea waves responsible for these microseisms in deep waters depends on the average group velocity $c_{sgw}$ by equation.

$$\nu = \frac{g}{2\pi c_{sgw}} \tag{1}$$

where $g$ is gravity acceleration. Being group velocities of sea waves controlled by the wind speed (500 cm/s on average in the Marmara region) the expected frequency for the lowest frequency peak is close to the observed one. The second peak may be due to the interference of these waves when they come from different directions. In this case, as observed, the expected periodicity is twice the frequency of the interfering waves (e.g., Longuet-Higgins, 1950).

The spectral amplitude variations of the two maxima and their possible frequency shifts could therefore correspond to the effects of meteorological variations at the surface, which cause changes in the duration and direction of the wind, producing changes in the amplitude and direction of the waves.

One can see that, despite of the fact that amplitude spectra relative to the noise level significantly change during the considered period along the three components, no significant change is observed in the HVSR curve. This curve shows a complex pattern with several maxima and minima with no apparent correlation with the noise level. The HVSR pattern in Fig. 2 has been revealed to be almost identical in all time intervals here considered (relative plots are reported in the supplementary material).

The main HVSR peaks at 3 Hz, 5 Hz and 9 Hz also show a marked directionality (Fig. 3) When computed by considering the projection of horizontal spectral components along different azimuths., HVSR peaks show maximum values in the southward direction, which indicates a significant heterogeneity of the ambient vibration wavefield (Fig. 3). This anisotropy could be the possible effect of the close presence of the NAF zone and directional seismic resonance phenomena induced by the energy trapping within the damaged rock zone due to the faulting process (e.g., Rovelli et al., 2002; Pischiutta et al., 2017).

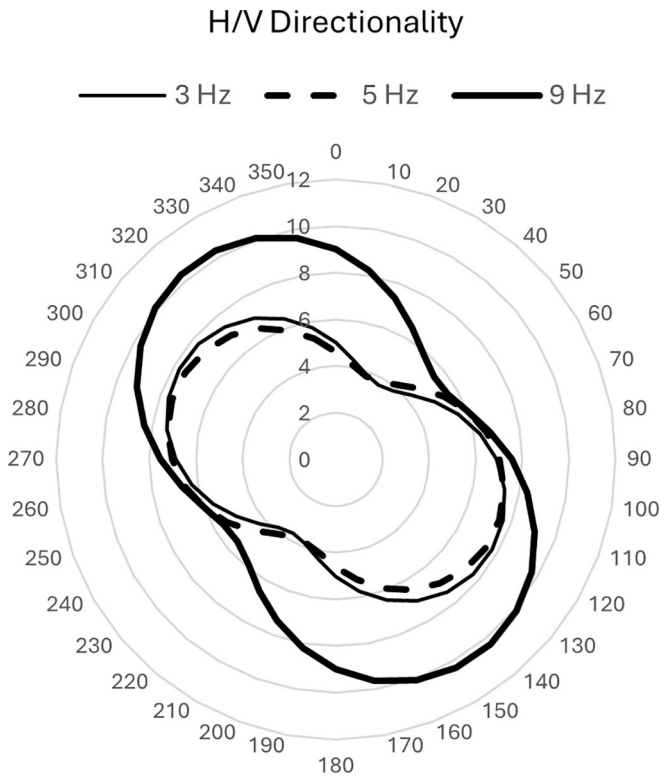


**Fig. 3.** Directionality of HVSR values corresponding to the three main spectral peaks at 3 Hz, 5 Hz and 9 Hz. The distance from the centre of the plot is proportional to the HVSR amplitude when considering the direction reported around the borders (degrees from North).

## 4. The possible impact of ocean dynamics on the HVSR pattern

Before any attempt of considering HVSR curve as representative to the subsoil conditions, potential disturbances induced by marine activity on the acquisition system must be evaluated.

These disturbances include, for example, the seabed currents that affect the sensor system, causing possible tilting of the OBS structure. For example, in the frequency band between 5 and 10 Hz, sea motion can induce 'parasitic' oscillations in the 'station-weight-unconsolidated sediment' system (Krylov et al., 2022). Other effects may be related to surface or internal wave movements of the sea (e.g., Jackson et al., 2012). The typical current speed ranges in the İzmit Gulf are between 5 and 19 cm/s (mean 11.3 cm/s) and between 5 and 9 cm/s (mean 6 cm/s) on the sea surface and the seabed, respectively (Algan et al., 1999). The maximum surface current speed is observed during February, July, and August, primarily in the western basin. The bottom current directions in the Darıca Basin vary seasonally but commonly exhibit a net flow towards the west and could be responsible for the marked anisotropy of the HVSR values at the peak frequencies. The tidal range in the İzmit Gulf is between 8 and 10 cm (Algan et al., 1999).

To evaluate the possible effects of these currents, seabed flow measurements conducted over the three days between March 10 and 13, 2010, were considered (Fig. 4). During the three days, marked flow variations were recorded, with values reaching up to 32 cm/s, well above the typical upper bound indicated above. These variations do not appear to be related to tidal motion, as they show no trace of the semi-diurnal periodicity characteristic of tidal flow. To assess the possible impact of these flow variations on the structure of the HVSR curves, the curves corresponding to periods of very high flow intensity (tentatively above 13 cm/s, i.e., twice maximum variations in quiet days) were compared with those obtained during periods of normal flow (Fig. 5). One can see that the flow intensity does not change significantly the frequency of HVSR maxima except for the very low-frequency part (< 0.2 Hz) and the relative amplitude of the maxima and minima.

When flow is below 13 cm/s the shape of the HVSR curve is identical to the one observed during other periods. When the flow exceeds this value, two main effects could be responsible for the observed pattern. The large increase of HVSR values below 0.2 Hz has been also observed inland and may result from gentle tilting of the sensor (e.g., Wielandt and Forbriger, 1999; Wielandt, 2002) due to the lateral pressure of the water flow on the OBS structure. The effect of water flow on the HVSR values above 0.5 Hz, may be the possible effect of flow variations not pertaining to the instrumental setup but rather to the level of stress induced on the subsurface, and thus its different response to the induced stress. A similar effect is observed in surface HVSR measurements outcropping sites, where the presence of strong winds produces significant effects on the HVSR measurement due to the interaction of wind with vegetation and topography (Chatelain et al., 2008).

Another possible effect potentially responsible for observed HVSR peaks could be related to effects induced by sea wave motion at the surface. The depth at which these effects can be observed is typically less than twice the wavelength (λ) of the ocean waves (e.g., Krogstad and Arntsen, 2017). Given that the measurement in this case is conducted at a depth of approximately 160 m, the waves responsible for the potential effects on the sensor should have a wavelength on the order of 300 m (long waves or 'swells'). The period $T$ of these waves can be determined using the dispersion relation (e.g., Nakata et al., 2019):

$$T = \sqrt{\frac{2\pi\lambda}{g}\frac{1}{tanh\left(\frac{2\pi}{\lambda}D\right)}} \quad (2)$$

where $D$ is the ocean depth and $\lambda$ is 2D (300 m in our case). With these figures, the period of wave potentially responsible for possible motions at the seabed is few seconds (i.e., around 0.1 Hz). This implies that seabed effects should only concern oscillation periods lower than 0.1 Hz, thus falling outside the scope of interest of this study.

An alternative possibility could be the presence of abyssal currents related to nonlinear internal waves (solitons) capable of generating flow variations that can exceed tens of meters per second (Jackson et al., 2012).

In summary, the analyses indicate a strong persistence of the HVSR curve shape, particularly regarding the frequencies at which the curve shows maxima or minima. However, the amplitude of.

these extreme values is strongly influenced by high flow values. In the presence of high seabed flow, the maxima observed at frequencies above 2 Hz are reduced at the expense of the maxima at very low frequencies. In general, the HVSR curves appear to reliably represent the

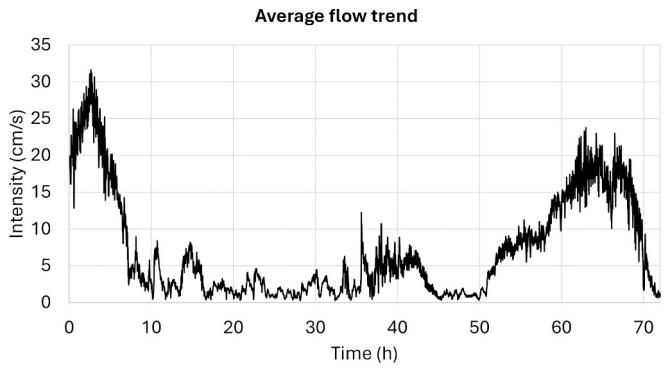


**Fig. 4.** Trend of the seafloor current speed measured at the seabed at the station, based on 5-min average.

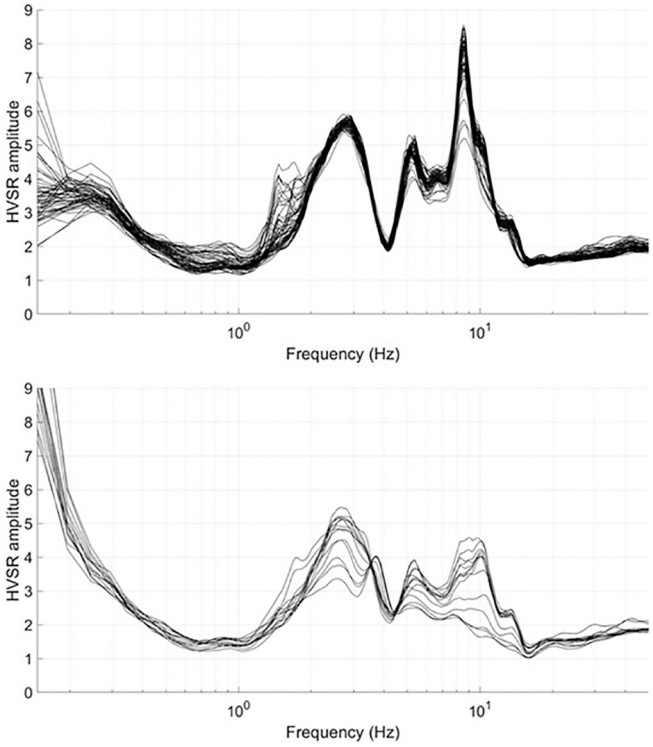


**Fig. 5.** 72-h record (March 10–13, 2010) illustrating the possible impact sea bottom water flow on the HVSR measurements. The upper inset shows the HVSR curve relative to the measurements from 06:00 p.m. on March 10th 2010 to midnight on March 13th and from 08:00 a.m. to 12:00 p.m. on March 13th, corresponding to the two periods during of low flow (< 13 cm/s). The lower inset shows HVSR curves relative to periods of high flow (> 13 cm/s) relative to the measurements from 12:00 p.m. to 6:00 p.m. on March 10th 2010, and from midnight on March 12th to 8:00 a.m. on March 13th 2010.

frequency response of the ground to the stresses induced by sea motion.

## 5. Body wave velocity profiles from HVSR curves

The hypothesis beyond the approach prosed by Albarello (2025) is correcting sea floor HVSR measurements by removing the effect of the overlying water column to obtain equivalent inland HVSR curves. This will allow the application to off-shore measurements of well established numerical tools developed to invert inland HVSR data.

By following the Herak model, the HVSR curve is considered as representative of natural resonance frequencies of the subsoil structure. Due to the 1D condition, compressional and shear strain disturbances, respectively considered as responsible for vertical and horizontal ground motion, travel independently within the layer stack. By solving homogeneous wave equations relative to these two components, imposing continuity of stress and displacements at each layer interface and free stress conditions at the surface, amplitude ratio between ground motion at the surface and at the bottom of stack can be computed (see, e.g., Kramer, 1996). In the assumption that input motion at the bottom of the layers stack are equal on average, the theoretical HVSR curve can be computed as the ratio between the seismic response of compressional and shear components of ground motion. This allows establishing a connection between HVSR and $V_s$ and $V_p$ profiles respectively representative of propagation effects of shear and compressional perturbations. A similar model has been considered by Brindisi et al. (2025) for the interpretation of HVSR curves corresponding to mud volcanoes in Northern Italy.

In this view, the spectral ratio $HV_{sf}$ at the seafloor is defined as the ratio between the spectral amplitudes of the horizontal $|U_{sf}|$ and vertical $|W_{sf}|$ ground motions at the bottom of the water column is

$$HV_{sf} = \frac{|U_{sf}|}{|W_{sf}|} \tag{3}$$

since the horizontal ground motion component is associated to shear strain, it will not be affected by the presence of the overlying water column. This is not the case of the horizontal component since compressive strain is transmitted to the water column and is affected by the interference of compressive waves reflected at the sea surface. If the water column was absent, the sea floor is outcropping and one would have

$$HV_{sf}^{out} = \frac{|U_{sf}|}{\left|W_{sf}^{out}\right|} \tag{4}$$

the effect of the interference of compressional waves within the water layer depends on the eater depth and at the sea bottom at the depth $h_w$ (is)

$$|W_{sf}| = I\left|cos\left(k_w^* h_w\right) + i\,\alpha_w^* sin\left(k_w^* h_w\right)\right| \tag{5}$$

where $I$ is the input motion at the seafloor,

$$\alpha_w^* = \frac{\rho_w V_w (1 + i\xi_w)}{\rho_{sf} V_{sf} (1 + i\xi_{sf})} \tag{6}$$

$$k_w^* = \frac{2\pi\nu}{V_w(1 + i\xi_w)} \tag{7}$$

where $V_w$ and $V_{sf}$ represent phase velocities of compressional waves in water and in the seafloor, the terms $\xi_w$ and $\xi_{sf}$are the respective damping factors and $\nu$ the frequency (see for the derivation, Kramer, 1996). In the case that the sea bottom was outcropping, due to the free surface effect, one has

$$\left|W_{sf}^{out}\right| = 2I \tag{8}$$

which implies

$$|W_{sf}| = \left|W_{sf}^{out}\right| \frac{\left|cos\left(k_w^* h_w\right) + i\,\alpha_w^* sin\left(k_w^* h_w\right)\right|}{2} \tag{9}$$

and

$$HV_{sf}^{out} = \frac{\left|cos\left(k_w^* h_w\right) + i\,\alpha_w^* sin\left(k_w^* h_w\right)\right|}{2} HV_{sf} \tag{10}$$

this allows removing the effect of the water column from the observed spectral ratio $HV_{sf}$.

Albarello (2025) has also shown that at the sea bottom conditions, this equation can be simplified in the simpler form

$$HV_{sf}^{out} = HV_{sf} \frac{1}{2} \sqrt{cos^2\left(\frac{2\pi\nu}{V_w} h_w\right) + \left(\frac{\rho_w V_w}{\rho_{sf} V_{sf}}\right)^2 sin^2\left(\frac{2\pi\nu}{V_w} h_w\right)} \tag{11}$$

It is worth to note that the procedure describe above, only attempts modelling the effect of the water column and in no way is able compensate the possible effects of the water dynamics on the ambient vibration wavefield or on the sensors itself. These possible role of these eventual biases should be evaluated after the application of the above correction.

## 6. Inversion of HVSR data at the Marmara Sea bottom site

By considering the approach described in Section 5, experimental HVSR curves have been corrected for the presence of the water column. To evaluate the possible impact the possible observational biases, average HVSR curves relative to low (< 0.13 m/s) and high (> 0.13 m/s) water flow conditions have been considered. To avoid the possible bias in the low frequency range due to the possible tilting effect during high flow periods, the HVSR curves in the frequency range 0.2–10 Hz have been considered only.

Each curve has been inverted by considering the numerical procedure implemented in *OpenHVSR* software (Bignardi et al., 2016). The inversion procedure requires initial guesses relative to the number of layers and, for each layer, body wave velocities ($V_p$, $V_s$), their respective attenuation factors ($\xi_p$, $\xi_s$), layer thickness ($H$), and density ($\rho$). The uppermost portion of the model was constrained using prior results from seismic investigation. Moreover, the velocity of the first $V_p$ layer was set close to 1500 m/s, which corresponds to the typical propagation velocity of seismic waves in water. This choice assumes that the first sedimentary layer in contact with the water column should not exhibit a $V_p$ value lower than that of water. We refer to Tary et al. (2012) and assume values for $V_p$, $V_s$, quality factors ($\xi_p$ and $\xi_s$), and density of 1550 m/s, 100 m/s, 0.05 and 0.05, and 1500 kg/m$^3$, respectively. Information on deeper sediment layers was inferred from the literature (Okyar et al., 2008; Kurt and Yücesoy, 2009). In-situ measurements of compressional (sound) wave velocity and attenuation, conducted on the seafloor at water depths ranging from 4 to 1100 m and across various sediment types, from coarse sand to clayey silt, allowed for the estimation of compressional-wave velocities, which are approximately 1600 m/s (Hamilton, 1972). Additionally, Hamilton (1976) estimated sediment bulk densities to be approximately 1500 kg/m$^3$. Finally, Hamilton (1977) reported shear-wave velocity measurements in water-saturated marine sediments, yielding average values around 250 m/s. The initial subsoil model is reported in Table 1.

The best fitting solution and the relative velocity profiles are reported in Fig. 6a and b respectively (referring to the high flow intensity period) and in Fig. 6c and d (referring to the low flow intensity period), as well as the final subsoil model (Table 1). The crucial outcome of the inversion result is that flow intensity does not significantly affect the subsoil response. Consequently, it can be stated that all the HVSR curves effectively represent the seismic response of the ground. A tentative evaluation of relevant uncertainty has been obtained by inverting the

**Table 1**
Initial and best fitting subsoil model. $V_p$ and $V_s$ correspond to *P*- and *S*-wave velocities; $\rho$ represents the density of the material; $H$ is the thickness of each layer; $\xi_p$ and $\xi_s$ are the shear and compressive wave damping factors.

| Initial subsoil model | | | | | |
|---|---|---|---|---|---|
| $V_p$ (m/s) | $V_s$ (m/s) | $\rho$ (g/cm$^3$) | $H$ (m) | $\xi_p$ | $\xi_s$ |
| 1550 | 100 | 1.5 | 4 | 0.05 | 0.05 |
| 1600 | 150 | 1.5 | 6 | 0.05 | 0.05 |
| 1650 | 200 | 1.5 | 65 | 0.03 | 0.03 |
| 1700 | 250 | 2.0 | 200 | 0.03 | 0.03 |
| 1700 | 250 | 2.0 | 350 | 0.02 | 0.02 |
| 1750 | 300 | 2.0 | – | – | – |
| Best fitting subsoil model | | | | | |
| $V_p$ (m/s) flow intensity: < 0.13 – > 0.13 | $V_s$ (m/s) flow intensity: < 0.13 – > 0.13 | $\rho$ (g/cm$^3$) flow intensity: < 0.13 – > 0.13 | $H$ (m) flow intensity: < 0.13 – > 0.13 | $\xi_p$ flow intensity: < 0.13 – > 0.13 | $\xi_s$ flow intensity: < 0.13 – > 0.13 |
| 51,535–1598 | 107–128 | 1.5–1.5 | 2–2 | 0.05–0.05 | 0.05–0.05 |
| 1958–2047 | 366–245 | 2.6–2.6 | 6–6 | 0.10–0.10 | 0.10–0.10 |
| 2717–2683 | 523–591 | 2.7–2.3 | 86–86 | 0.02–0.02 | 0.03–0.02 |
| 1915–1933 | 370–377 | 2.1–2.1 | 80–80 | 0.04–0.04 | 0.01–0.05 |
| 2143–2029 | 764–725 | 1.4–1.4 | 322–322 | 0.01–0.01 | 0.01–0.01 |
| 2500–2358 | 907–931 | 1.5–1.5 | – | – | – |

HVSR curves relative to maximum and minimum values at each frequency, derived from the complete set of measurement time windows acquired during periods of high and low flow intensity, respectively.

The resulting $V_p$ profile reveals a seismic impedance contrast at approximately 10 m depth, which may correspond to the base of the marine unit described by Gasperini et al. (2012a), embedded within Holocenic sedimentary sequence as discussed in Section 2. The velocity inversion observed at greater depths could mark the transition to Sequence 1. Forward modelling of body wave propagation supports the hypothesis that the spectral anomaly, characterized by a minimum around 0.8 Hz, arises from an impedance contrast at approximately 495 m depth possibly representative of the contact between the Quaternary depositional sequences and the underlying Triassic formations. The marked change in the $V_p$ and $V_s$ ratios can be interpreted following Tinivella (2002), who suggests that a high Poisson's ratio, exceeding 0.3, is indicative of poorly consolidated materials.

## 7. Modelling body waves velocity profiles by the Biot-Gassmann theory

The intent of this study is to apply Brindisi et al. (2025) approach for estimating potential gas concentration based on compressional and shear wave velocity profiles. Given the absence of any evidence indicating lateral variations in the lithostratigraphic framework between the gas-emitting area and adjacent regions, we adopt reference $V_p$ and $V_s$ values from the literature (Hamilton, 1972; Hamilton, 1977) to constrain the surrounding area. This approach is aimed at assessing the applicability of the Brindisi et al. (2025) model to this site.

To evaluate the applicability of this method, we refer to the Biot-Gassmann theory formulated by Lee (2004), hereafter referred to as BGTL. Following the considerations proposed by Tinivella (2002), we utilize the physical parameters derived from the modelling of HVSR curves to understand whether a uniform or patchy gas distribution is likely within the pore space (Lee, 2004). On this basis, we examined the body wave velocity profiles displayed in Fig. 6, considering the different lithotypes present in the subsoil and the corresponding impedance contrasts.

Assuming the absence of lithological variations between the vent-emitting area and its surroundings, the bulk and shear moduli of the host material have been derived from estimated $V_p$, $V_s$, and density values Mari (2019).

In the BGTL model, the $V_p$ and $V_s$ profiles of fluid-saturated sediments are controlled by porosity ($\phi$), water saturation ($S_w$), clay volume content ($C_v$), and two calibration parameters, denoted as '*e*' and '*m*'. The parameter '*m*' is related to the degree of sediment consolidation, whereas '*e*' reflects the mode of gas saturation in the pore space (patchy or regular), as defined by Tinivella (2002). According to her, Poisson's Ratio below 0.3 is indicative of regular saturation, while exceeding 0.3 suggests patchy saturation. Acceptable ranges for these variables, according to the specific lithologies present in the area, are provided by Lee (2004) and Yu et al. (1993). Nevertheless, $\phi$ and $S_w$ emerge as the most influential parameters in the modelling process.

The values of the free parameters ($\phi$, $S_w$, $C_v$, $e$, and $m$) were derived through an inversion process aimed at optimally fitting the $V_p$ and $V_s$ profiles shown in Fig. 6.

The results of the BGTL modelling indicate a consistent $C_v$ and $\phi$ of 0.1 % throughout the 0–495 m depth interval. The calibration parameter '*m*' varies from a value of 2 in the uppermost 10 m to 6 for the remainder of the profile. The parameter '*e*' remains constant at a value of 2 across the entire profile, reflecting the high Poisson's ratio (> 0.3) observed, and indicating patchy gas saturation conditions. $S_w$ decreases with depth, estimated at 0.9 % in the upper 95 m and dropping to 0.5 % between 95 m and 495 m. It is worth noting that the saturation model contains fewer layers than the velocity model because it is derived from the BGTL modelling results, which highlight only contrasts resulting from variations in subsurface fluid saturation. In our study area, such variations are evident only at approximately 100 m depth: at this depth, the gas saturation within the pores increases significantly, while the water saturation decreases. This observation is fully consistent with the reduction in P-wave velocity observed at the same depth (Fig. 6b and d).

This modelling approach ultimately allows for a quantitative estimation of gas saturation ($S_g$) levels, expressed as percentages, within the study area. The corresponding $S_w$ and $S_g$ profiles along the subsurface section are shown in Fig. 6e and f respectively.

## 8. Conclusions

It has been proposed that horizontal to vertical spectral ratio of ambient vibrations measured at the sea bottom can be used to constrain the local seismostratigraphical configuration. In the case study here considered, it has been suggested that water high flow may affect the HVSR pattern (due e.g., to the possible tilting effect on the sensors) mainly when very low frequencies (< 0.2 Hz) are of concern. For higher frequencies, however, these effects manly result in minor changes in the peaks amplitudes leaving unchanged the respective frequencies. In this view, we have assumed that a physical link can be established between the HVSR curve above 0.2 Hz and a 1D subsoil configuration in terms of $V_s$ and $V_p$ profiles, in a way like that considered for the analysis of HVSR data inland. A new correction procedure has been proposed here to account for the seismic resonance effects of the water column and retrieve an HVSR curve like the one observed inland. In this way, inversion procedures commonly considered for the interpretation of HVSR inland can be applied to sea bottom observations, by opening new perspectives to the use of OBS data. In the lack of independent evaluations of the $V_s$ and $V_p$ profiles, the one here presented should only be considered as tentative and could be considered as a first step towards a full exploitation of sea bottom seismic measurements. The good fitting between the body waves velocity profiles and those inferred by the BGTL modelling suggests that gas plays a significant role in this area, indeed especially in depth (from 175 to 495 m) it is preliminarily estimated to cover the 50 % of the pore space.

In conclusion, our results support the feasibility of using ocean bottom seismic measurements of ambient vibrations to investigate the seismostratigraphical configuration of the subsoil. Furthermore, as suggested in this study, this approach can also be used to estimate gas concentration within a reservoir system through BGTL modelling, thereby validating the effectiveness of this combined method.

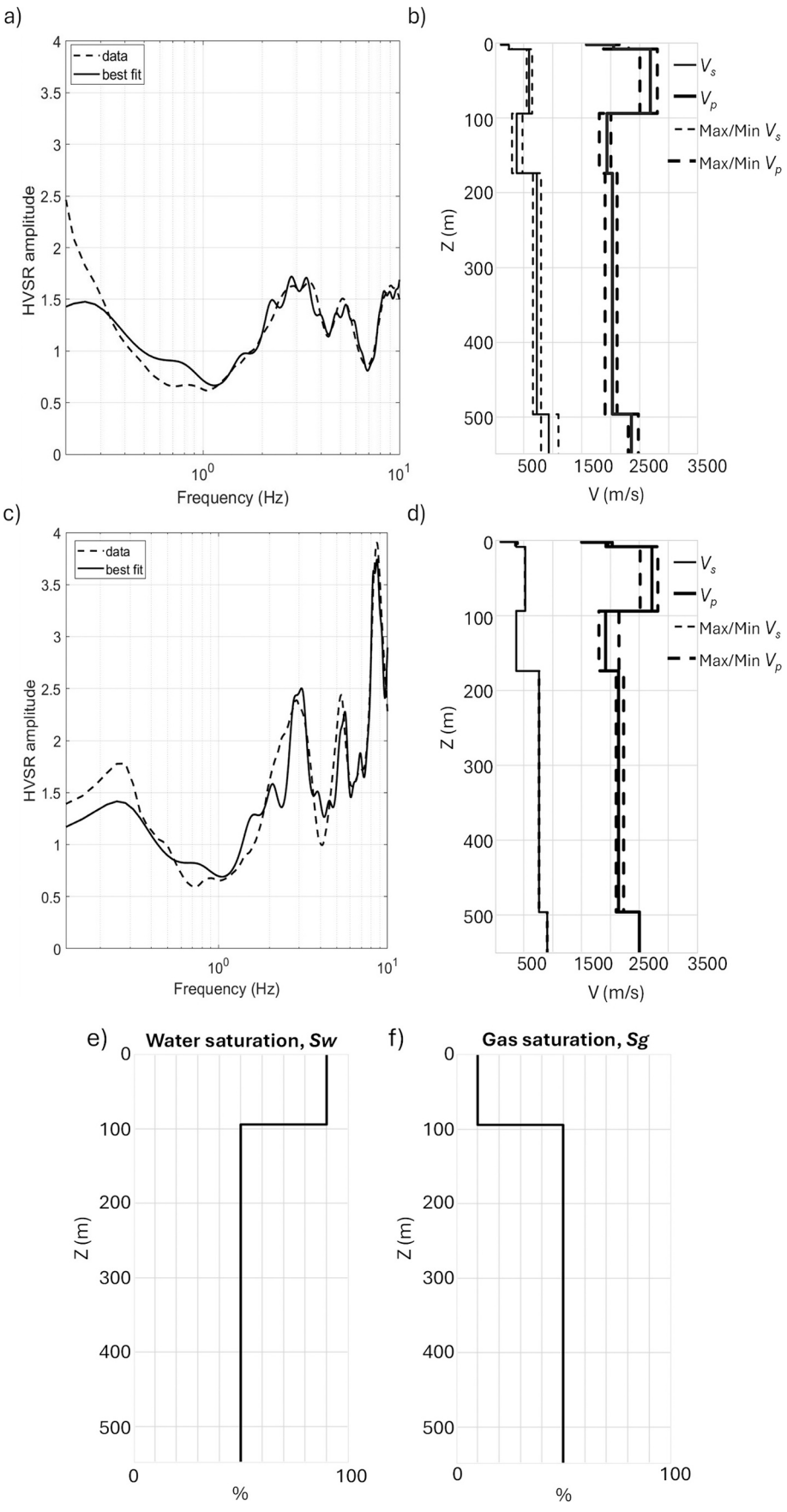


*(caption on next page)*

**Fig. 6.** Inversion of the HVSR experimental curves after the removal of the water column effects. **a)** Comparison between the best fitting HVSR curve obtained by the inversion procedure (solid line) and the data, represented by the mean HVSR curve (dashed line), corresponding to periods of high flow intensity. **b)** The solid black line represents the $V_s$ profile considered to obtain the best fitting curve in **(a)**, the dashed black lines represent the profile of the maximum and minimum $V_s$ value at each depth. The solid bold black line represents the $V_p$ profile considered to obtain the best fitting curve in **(a)**, the dashed bold black lines represent the profile of the maximum and minimum $V_p$ value at each depth. **(c-d)** Results corresponding to periods of low flow intensity, following the same layout as **(a)** and **(b)**. **e)** Water saturation ($S_w$) profile expressed in percentage obtained by the BGTL modelling. **f)** Gas saturation ($S_g$) profile expressed in percentage obtained by the BGTL modelling.

## CRediT authorship contribution statement

**A. Brindisi:** Writing – review & editing, Writing – original draft, Investigation, Data curation, Conceptualization. **S. D'Amico:** Writing – review & editing, Data curation, Conceptualization. **L. Beranzoli:** Writing – review & editing, Data curation, Conceptualization. **D. Embriaco:** Writing – review & editing, Data curation. **A. Giuntini:** Writing – review & editing, Data curation. **D. Albarello:** Writing – review & editing, Writing – original draft, Supervision, Methodology, Conceptualization.

## Declaration of competing interest

Dario Albarello reports administrative support was provided by University of Siena Department of Physics Earth and Environmental Sciences. Dario Albarello reports a relationship with University of Siena Department of Physics Earth and Environmental Sciences that includes: board membership. None If there are other authors, they declare that they have no known competing financial interests or personal relationships that could have appeared to influence the work reported in this paper.

## Acknowledgements

Many thanks are due to the three anonymous reviewers for their comments and fruitful suggestions, which gave us the opportunity to largely improve the text.

## Appendix A. Supplementary data

Supplementary data to this article can be found online at https://doi.org/10.1016/j.jappgeo.2025.106025.

## Data availability

Data will be made available on request.

## References

Albarello, D., 2025. Reducing Horizontal to Vertical Spectral Ratios of ambient vibrations measured at the sea bottom to inland equivalent values. Mar.Geophys. Res. 46, 29. https://doi.org/10.1007/s11001-025-09591-6.

Albarello, D., Herak, M., Lunedei, E., Paolucci, E., Tanzini, A., 2023. Simulating H/V spectral ratios (HVSR) of ambient vibrations: a comparison among numerical models. Geophys. J. Int. 234 (2), 870–878. https://doi-org.ezproxy.unibo.it/10.1093/gji/ggad109.

Algan, O., Altıok, H., Yüce, H., 1999. Seasonal variation of suspended particulate matter in two-layered Izmit Bay, Turkey. Estuar. Coast. Shelf Sci. 49 (2), 235–250. https://doi.org/10.1006/ecss.1999.0494.

Antunes, V., Planès, T., Obermann, A., Panzera, F., D'Amico, S., Mazzini, A., Lupi, M., 2022. Insights into the dynamics of the Nirano Mud Volcano through seismic characterization of drumbeat signals and V/H analysis. J. Volcanol. Geotherm. Res. 431, 107619. https://doi.org/10.1016/j.jvolgeores.2022.107619.

Beranzoli, L., Braun, T., Calcara, M., Casale, P., De Santis, A., D'Anna, G., Di Mauro, D., Etiope, G., Favali, P., Fuda, J.L., Frugoni, F., 2003. Mission results from the first GEOSTAR observatory (Adriatic Sea, 1998). Earth Planets Space 55, 361–373. https://doi.org/10.1186/BF03351770.

Bignardi, S., Mantovani, A., Zeid, N.A., 2016. OpenHVSR: imaging the subsurface 2D/3D elastic properties through multiple HVSR modeling and inversion. Comput. Geosci. 93, 103–113. https://doi.org/10.1016/j.cageo.2016.05.009.

Brindisi, A., Paolucci, E., Carfagna, N., Albarello, D., 2025. Passive seismic measurements to characterize gas reservoirs in a mud volcano field in Northern Italy. Mar. Pet. Geol. 173, 107275. https://doi.org/10.1016/j.marpetgeo.2024.107275.

Çetin, O., Çetin, T., Ukav, İ., 1995. Electron spin resonance (ESR) dating of fossil mollusc shells observed in Quaternary sequence in the Gulf of İzmit (Hersek Burnu-Kaba Burun). In: Meriç, E. (Ed.), Quaternary Sequence in the Gulf of İzmit. Deniz Harp Okulu Komutanlığı Basımevi, İstanbul, Turkey, pp. 269–275. https://doi.org/10.1007/s11001-008-9049-6.

Chatelain, J.L., Guillier, B., Cara, F., Duval, A.M., Atakan, K., Bard, P.Y., Wp02 Sesame Team, 2008. Evaluation of the influence of experimental conditions on H/V results from ambient noise recordings. Bull. Earthq. Eng. 6, 33–74. https://doi.org/10.1007/s10518-007-9040-7.

Comina, C., Di Chiara, G., Foti, S., 2023. On the direct estimation of bedrock depth and time-weighted average VS from surface waves dispersion and HVSR curves. J. Appl. Geophys. 215, 105086. https://doi.org/10.1016/j.jappgeo.2023.105086.

Embriaco, D., Marinaro, G., Frugoni, F., Monna, S., Etiope, G., Gasperini, L., Polonia, A., Del Bianco, F., Çağatay, M.N., Ulgen, U.B., Favali, P., 2014. Monitoring of gas and seismic energy release by multiparametric benthic observatory along the North Anatolian Fault in the Sea of Marmara (NW Turkey). Geophys. J. Int. 196 (2), 850–866. https://doi.org/10.1093/gji/ggt436.

Farazi, A.H., Ito, Y., Garcia, E.S.M., Lontsi, A.M., Sánchez-Sesma, F.J., Jaramillo, A., Ohyanagi, S., Hino, R., Shinohara, M., 2023. Shear wave velocity structure at the Fukushima forearc region based on H/V analysis of ambient noise recordings by ocean bottom seismometers. Geophys. J. Int. 233 (3), 1801–1820. https://doi.org/10.1093/gji/ggad028.

Favali, P., Beranzoli, L., Anna, G.D., Gasparoni, F., Marvaldi, J., Clauss, G., Gerber, H.W., Nicot, M., Marani, M.P., Gamberi, F., 2006. A fleet of multiparameter observatories for geophysical and environmental monitoring at seafloor. Ann. Geophys. 49 (2–3). https://doi.org/10.4401/ag-3126.

García-Jerez, A., Piña-Flores, J., Sánchez-Sesma, F.J., Luzón, F., Perton, M., 2016. A computer code for forward calculation and inversion of the H/V spectral ratio under the diffuse field assumption. Comput. Geosci. 97, 67–78. https://doi.org/10.1016/j.cageo.2016.06.016.

Gasperini, L., Polonia, A., Del Bianco, F., Etiope, G., Marinaro, G., Favali, P., Italiano, F., Çağatay, M.N, 2012. Gas seepages and seismogenic structures along the North Anatolian Fault in the Eastern Marmara Sea. Geochem. Geophys. Geosyst., 13, Q10018, doi:https://doi.org/10.1029/2012GC004190.

Grassi, S., De Guidi, G., Patti, G., Brighenti, F., Carnemolla, F., Imposa, S., 2022. 3D subsoil reconstruction of a mud volcano in Central Sicily by means of geophysical surveys. Acta Geophys. 70 (3), 1083–1102. https://doi.org/10.1007/s11600-022-00774-y.

Hamilton, E.L., 1972. Compressional-wave attenuation in marine sediments. Geophysics 37 (4), 620–646. https://doi.org/10.1190/1.1440287.

Hamilton, E.L., 1976. Variations of density and porosity with depth in deep-sea sediments. J. Sediment. Res. 46 (2), 280–300. https://doi.org/10.1306/212F6F3C-2B24-11D7-8648000102C1865D.

Hamilton, E.L., 1977. Shear-wave velocity versus depth in marine sediments: a review. Log. Anal. 18 (01).

Hasselmann, K., 1963. A statistical analysis of the generation of microseisms. Rev. Geophys. 1 (2), 177–210. https://doi.org/10.1029/RG001i002p00177.

Herak, M., 2008. ModelHVSR-A Matlab tool to model horizontal-to-vertical spectral ratio of ambient noise. Comput. Geosci. 34, 1514–1526. https://doi.org/10.1016/j.cageo.2007.07.009.

Huerta-Lopez, C., Pulliam, J., Nakamura, Y., 2003. In situ evaluation of shear-wave velocities in seafloor sediments with a broadband oceanbottom seismograph. Bull. Seismol. Soc. Am. 93 (1), 139–151. https://doi.org/10.1785/0120010276.

Jackson, C.R., Da Silva, J.C.B., Jeans, G., 2012. The generation of nonlinear internal waves. Oceanography 25 (2), 108–123. https://doi.org/10.5670/oceanog.2012.46.

Keskinsezer, A., Karaaslan, H., Silahtar, A., Beyhan, G., 2023. The soil characterization of the region between the Maltepe-Beykoz Fault and the Marmara Sea in İstanbul (Türkiye) with the integrated HVSR (Nakamura technique) and MASW method. J. Appl.Geophys. 219, 105245. https://doi.org/10.1016/j.jappgeo.2023.105245.

Kramer, S.L., 1996. Geotechnical Earthquake Engineering. Prentice Hall, New Jersey, NJ, USA.

Krogstad, H.E., Arntsen, Ø.A., 2017. Linear Wave Theory, Part A. regular Waves, Norwegian University of Science and Technology, Trondheim, Norway, available online at http://folk.ntnu.no/oivarn/hercules_ntnu/LWTcourse/lwt_new_2000_Part_A.pdf (retrieved on Feb 4th, 2017) last modified on April 5.

Krylov, A.A., Kulikov, M.E., Kovachev, S.A., Medvedev, I.P., Lobkovsky, L.I., Semiletov, I. P., 2022. Peculiarities of the HVSR method application to seismic records obtained by Ocean-Bottom seismographs in the arctic. Appl. Sci. 12 (19), 9576. https://doi.org/10.3390/app12199576.

Kurt, H., Yücesoy, E., 2009. Submarine structures in the Gulf of İzmit, based on multichannel seismic reflection and multibeam bathymetry. Mar. Geophys. Res. 30 (2), 73–84. https://doi.org/10.1007/s11001-009-9068-y.

Kuşçu, I., Okamura, M., Matsuoka, H., Gokasan, E., Awata, Y., Tur, H., Simsek, M., Keçer, M., 2005. Seafloor gas seeps and sediment failures triggered by the August 17, 1999 earthquake in the Eastern part of the Gulf of Izmit, Sea of Marmara, NW Turkey. Mar. Geol. 215, 193–214. https://doi.org/10.1016/j.margeo.2004.12.002.

Lambert, M., Schmalholz, S.M., Podladchikov, Y.Y., Saenger, E.H., 2007. Low frequency anomalies in spectral ratios of single station microtremor measurements: observations across an oil and gas field in Austria. In: 77th Annual International Meeting, SEG, Extended Abstracts, pp. 1352–1356. https://doi.org/10.1190/1.2792751.

Lee, M.W., 2004. Elastic velocities of partially gas-saturated unconsolidated sediments. Mar. Pet. Geol. 21 (6), 641–650. https://doi.org/10.1016/j.marpetgeo.2003.12.004.

Lepore, S., Grad, M., 2020. Relation between ocean wave activity and wavefield of the ambient noise recorded in northern Poland. J. Seismol. 24, 1075–1094. https://doi.org/10.1007/s10950-020-09963-y.

Longuet-Higgins, M.S., 1950. A theory of the origin of microseisms. Philosophical Trans. R. Soc. Lond. Series A, Math. Phys. Sci. 243 (857), 1–35. https://doi.org/10.1098/rsta.1950.0012.

Lontsi, A.M., García-Jerez, A., Molina-Villegas, J.C., Sánchez-Sesma, F.J., Molkenthin, C., Ohrnberger, M., Krüger, F., Wang, R., Fäh, D., 2019. A generalized theory for full microtremor horizontal-to-vertical [H/V(z, f)] spectral ratio interpretation in offshore and onshore environments. Geophys. J. Int. 218, 1276–1297. https://doi.org/10.1093/gji/ggz223.

Mari, J.L., 2019. Wave propagation. In: Mendes, Mari (Ed.), Seismic Imaging: A Practical Approach, 206. https://doi.org/10.1051/978-2-7598-2351-2.c003. EDP Sciences.

Mele, M., Bersezio, R., Bini, A., Bruno, M., Giudici, M., Tantardini, D., 2021. Subsurface profiling of buried valleys in central alps (northern Italy) using HVSR single-station passive seismic. J.Appl.Geophys. 193, 104407. https://doi.org/10.1016/j.jappgeo.2021.104407.

Mitchum, R.M., Vail, P.R., Sangree, J.B., 1977. Seismic stratigraphy and global changes of sea level, part 6: stratigraphic interpretation of seismic reflection patterns in depositional sequences. In: Payton, C.E. (Ed.), Seismic Stratigraphy-Applications to Hydrocarbon Exploration. AAPG Mem., 26, Tulsa, Oklahoma, pp. 117–133. https://doi.org/10.1306/M26490C8.

Molnar, S., Sirohey, A., Assaf, J., Bard, P.Y., Castellaro, S., Cornou, C., Cox, B., Guillier, B., Hassani, B., Kawase, H., Matsushima, S., Sánchez-Sesma, F.J., Yong, A., 2022. A review of the microtremor horizontal-to-vertical spectral ratio (MHVSR) method. J. Seismol. 26 (4), 653–685. https://doi.org/10.1007/s10950-021-10062-9.

Monna, S., Frugoni, F., Montuori, C., Beranzoli, L., Favali, P., 2005. High quality seismological recordings from the SN-1 deep seafloor observatory in the Mt. Etna region. Geophys. Res. Lett. 32 (7). https://doi.org/10.1029/2004GL021975.

Mulargia, F., 2012. The seismic noise wavefield is not diffuse. J. Acoust. Soc. Am. 131 (4), 2853–2858. https://doi.org/10.1121/1.3689551.

Muyzert, E., 2007. Seabed property estimation from ambient-noise recordings: part 2—Scholte-wave spectral-ratio inversion. Geophysics 72 (4), U47–U53. https://doi.org/10.1190/1.2719062.

Nakata, N., Gualtieri, L., Fichtner, A. (Eds.), 2019. Seismic Ambient Noise. Cambridge University Press.

Okyar, M., Pinar, A., Tezcan, D., Kamaci, Z., 2008. Late quaternary seismic stratigraphy and active faults of the Gulf of Izmit (NE Marmara Sea). Mar. Geophys. Res. 29, 89–107. https://doi.org/10.1007/s11001-008-9049-6.

Overduin, P.P., Haberland, C., Ryberg, T., Kneier, F., Jacobi, T., Grigoriev, M.N., Ohrnberger, M., 2015. Submarine permafrost depth from ambient seismic noise. Geophys. Res. Lett. 42 (18), 7581–7588. https://doi.org/10.1002/2015GL065409.

Panzera, F., Sicali, S., Lombardo, G., Imposa, S., Gresta, S., D'Amico, S., 2016. A microtremor survey to define the subsoil structure in a mud volcanoes area: the case study of Salinelle (Mt. Etna, Italy). Environ. Earth Sci. 75, 1–13. https://doi.org/10.1007/s12665-016-5974-x.

Picozzi, M., Parolai, S., Albarello, D., 2005. Statistical analysis of noise horizontal to vertical spectral ratios (HVSR). Bull. Seismol. Soc. Am. 95, 1779–1786. https://doi.org/10.1785/0120040152.

Pischiutta, M., Fondriest, M., Demurtas, M., Magnoni, F., Di Toro, G., Rovelli, A., 2017. Structural control on the directional amplification of seismic noise (Campo Imperatore, Central Italy). Earth Planet. Sci. Lett. 471, 10–18. https://doi.org/10.1016/j.epsl.2017.04.017.

Polonia, A., Gasperini, L., Amorosi, A., Bonatti, E., Bortoluzzi, G., Cagatay, N., Capotondi, L., Cormier, M.H., Gorur, N., McHugh, C., Seeber, L., 2004. Holocene slip rate of the North Anatolian Fault beneath the Sea of Marmara. Earth Planet. Sci. Lett. 227 (3–4), 411–426. https://doi.org/10.1016/j.epsl.2004.07.042.

Rovelli, A., Caserta, A., Marra, F., Ruggiero, V., 2002. Can seismic waves be trapped inside an inactive fault zone? The case study of Nocera Umbra, Central Italy. Bull. Seim. Soc. Am. 92 (6), 2217–2232. https://doi.org/10.1785/0120010288.

Saenger, E.H., Schmalholz, S.M., Lambert, M.A., Nguyen, T.T., Torres, A., Metzger, S., Habiger, R.M., Müller, T., Rentsch, S., Méndez-Hernández, E., 2009. A passive seismic survey over a gas field: Analysis of low-frequency anomalies. Geophysics 74 (2), O29–O40. https://doi.org/10.1190/1.3078402.

Sánchez-Sesma, F.J., 2017. Modeling and inversion of the microtremor H/V spectral ratio: physical basis behind the diffuse field approach. EPS 69 (1), 92. https://doi.org/10.1186/s40623-017-0667-6.

Shynkarenko, A., Lontsi, A.M., Kremer, K., Bergamo, P., Hobiger, M., Halló, M., Fäh, D., 2021. Investigating the subsurface in a shallow water environment using array and single-station ambient vibration techniques. Geophys. J. Int. 227 (3), 1857–1878. https://doi.org/10.1093/gji/ggab314.

Tary, J.B., Geli, L., Guennou, C., Henry, P., Sultan, N., Çağatay, N., Vidal, V., 2012. Microevents produced by gas migration and expulsion at the seabed: a study based on sea bottom recordings from the Sea of Marmara. Geophys. J. Int. 190 (2), 993–1007. https://doi.org/10.1111/j.1365-246X.2012.05533.x.

Tinivella, U., 2002. The seismic response to over-pressure versus gas hydrate and free gas concentration. J. Seism. Explor. 11 (3), 283–305.

Wathelet, M., Chatelain, J.L., Cornou, C., Giulio, G.D., Guillier, B., Ohrnberger, M., Savvaidis, A., 2020. Geopsy: a user-friendly open-source tool set for ambient vibration processing. Seismol. Res. Lett. 91 (3), 1878–1889. https://doi.org/10.1785/0220190360.

Webb, S.C., 1998. Broadband seismology and noise under the ocean. Rev. Geophys. 36 (1), 105–142. https://doi.org/10.1029/97RG02287.

Wielandt E., 2002. Seismic sensors and their calibration. In: P. Bormann and E. Bergmann (editors), New Manual of Seismological Observatory Practice, GeoForschungsZentrum Potsdam, Germany. <http://www.geophys.uni-stuttgart.de/seismometry/man html/index.html>, <http://www.geophys.uni-stuttgart.de/downloads/Postscript-files>.

Wielandt, E., Forbriger, T., 1999. Near-field seismic displacement and tilt associated with the explosive activity of Stromboli. Ann. Gofis. 42 (3), 407–416.

Yu, C., Cheng, J.J., Jones, L.G., Wang, Y.Y., Faillace, E., Loureiro, C., Chia, Y.P., 1993. Data Collection Handbook to Support Modeling the Impacts of Radioactive Material in Soil, Vols. No. ANL/EAIS–8. Argonne National Lab.